ADVANCED THEORY AND SIMULATIONS
www.advtheorysimul.com

Computing the Lattice Thermal Conductivity of Small-Molecule Organic Semiconductors: A Systematic Comparison of Molecular Dynamics Based Methods

*Alexandre Vercouter, Vincent Lemaur, Claudio Melis, and Jérôme Cornil**

While the Green-Kubo and non-equilibrium molecular dynamics methods have been compared quite extensively to calculate the thermal conductivity in inorganic compounds, there is currently a lack of comparison of these algorithms with the more recently developed approach-to-equilibrium molecular dynamics (AEMD) method for other types of materials such as organic semiconductors. To fill this gap, this article reports a theoretical description of thermal transport in single crystals made of terthiophene as prototypical system based on the three most popular molecular dynamics approaches. A systematic comparison of the computed values of thermal conductivity and its anisotropy is carried out and the strengths and weaknesses associated with each method are discussed. Although the three algorithms give essentially the same trends, this study points to the "AEMD" approach as the most suitable compromise between accuracy and computing cost. On the material aspects, the theoretical modeling yields an anisotropic character of the thermal transport in crystals whose out-of-plane thermal conductivity component is approximately twice larger than the in-plane components. The AEMD approach is further used to investigate the influence of temperature on thermal transport in terthiophene. The trends are utterly rationalized by relying on the concepts of phonon mean free paths and phonon group velocities.

1. Introduction

Achieving a comprehensive understanding of heat transport characteristics in solid-state systems is commonly regarded as a key feature for a broad range of domains, including thermal management in micro- and opto-electronic architectures, energy co-generation or harvesting as well as thermoelectric energy conversion to name but a few.[1,2] In analogy with electrons and photons, phonons have also been explored as both carriers and storers of information in computing systems through the new field of "phononics."[3,4] In the past few years, drastic efforts have been made to both computationally and experimentally provide new insights on thermal transport for the tailored design of novel materials; such improvements could allow to meet requirements for cutting-edge technologies like the "internet of things."[5] However, the difficulties faced by the scientific community when probing thermal capacities of solids are so high that this task can be fairly well described as much as an exciting than daunting challenge. From the experimental viewpoint, some studies based either on the 3ω method[6] or on frequency/time-domain thermoreflectance techniques[7,8] have recently provided measurements of phonon mean free paths[9] (MFPs), hence allowing their use for an in-depth analysis of heat transport mechanisms. Unfortunately, this property alone appears to be insufficient for the fully qualitative interpretation of experimental data in the very few cases reported so far.[10]

On the theoretical side, a deep description of heat transport phenomena in solid systems at both the micro- and the nanoscopic scales has been attempted by the development of several computational models over the last two decades. This has witnessed the emergence of a class of ab initio methods solving exactly (self-consistent or variational approaches)[11,12] or approximately (in the single mode approximation or SMA)[13] the Boltzmann Transport Equation (BTE)[14] which was initially formulated by Peierls in 1929. Basically, the BTE framework relies on a phonon picture in which heat conduction is assumed to be fully determined by phonon scattering processes and their associated properties such as phonon frequencies, phonon scattering rates, and group velocities. To this aim, a clear and suitable description of these quantities can be reached by exploiting the derivatives of the potential energy with respect to atomic displacements. More precisely, accurate harmonic and anharmonic interatomic force constants (IFCs) are typically extracted from first principles calculations based on compression sensing[15] or density functional perturbation (DFT) theory.[16] However, the ab initio

A. Vercouter, V. Lemaur, J. Cornil
Laboratory for Chemistry of Novel Materials
University of Mons
Mons 7000, Belgium
E-mail: jerome.cornil@umons.ac.be
C. Melis
Dipartimento di Fisica
Università di Cagliari
interna Policlinico Universitario, Monserrato, CA 09042, Italy

The ORCID identification number(s) for the author(s) of this article can be found under https://doi.org/10.1002/adts.202200892

DOI: 10.1002/adts.202200892

evaluation of IFCs is often so computationally demanding that solving of BTE usually needs to be truncated to the third (or at most fourth) order derivatives, thereby limiting their domain of applicability to the study of conductive heat transport at very low temperatures (i.e., far below the melting point). In any case, one of the major roadblocks which makes the applicability of such a sophisticated quantum simulation framework particularly challenging for the investigation of thermal transport properties in organic compounds is their high computational workload. Indeed, the use of DFT-based approaches remains restricted to perfectly ordered systems including no more than a few hundred atoms, therefore rendering first-principles calculations inappropriate for the investigation of more realistic disordered structures like molecular crystals, usually displaying non-periodic defects such as vacancies, dopants, etc. Furthermore, this approach cannot be employed for reliably modeling the thermal conductivity of compounds at high temperatures for which higher-than-third-order anharmonic phonon-phonon interactions have to be taken into account.

As an alternative to this first class of computational tools, a second approach[17] based on the evaluation of actual atomic trajectories in the real space has been developed. Herein, the classical molecular dynamics (MD) framework takes advantage of the full anharmonicity of empirical many-body potentials to assess the heat conduction properties of a given system via the computation of instantaneous heat fluxes or local temperatures. In contrast to first-principles approaches, MD methods can be exploited on virtually any complex material in whatever state of matter or thermodynamic condition; the latter is strictly ruled by the nature of the statistical ensemble initially set as input. While performing ab initio calculations on organic supercells of relevant size still remains beyond the reach of currently available computational resources, MD can be extensively applied to systems containing up to several millions of atoms with simulation times extending over one hundred of nanoseconds. Nevertheless, some other concerns have been raised in the past about the ability of empirical potentials to reliably capture phonon properties, such as the phonon spectrum (especially in the high frequency range). In addition, MD should -in principle- be restrained to simulations performed at high temperatures where quantum effects are more limited. This is motivated by the fact that MD follows a classical (Boltzmann) distribution while ab initio calculations mainly rely on quantum (Bose-Einstein) phonon statistics. A strong asset for MD simulations is the fact that heat transport is typically dominated by low energy lattice phonons, thus minimizing the impact of quantum effects. When applied to molecular crystals, as it is the case here, the force field used should be critically validated to ensure that the system vibrates around an equilibrium geometry close to the experimental X-ray structure and ideally that the computed lattice phonon frequencies and displacements match those calculated with sophisticated quantum-chemical approaches or reproduce experimental Raman or neutron scattering spectra.[18,19] When using force field- or DFT-based calculations, a first step is to minimize the crystal unit cell at the chosen theoretical level in order to fluctuate around the equilibrium geometry and avoid negative vibrational frequencies. Nevertheless, a key issue is to make sure that the relaxed structure does not deviate too much from the X-ray crystalline structure, which would have in turn also a profound impact on the phonon density of states and related properties.[20] When the unit cell geometry is properly described, it is our experience that lattice phonons computed at the force field versus quantum level behave collectively in a very similar way.[21] We will not dwell further on this issue in the present paper whose main goal is to compare three different algorithms using the same force field.

Basically, the set of MD-based methodologies that can be employed to compute the lattice thermal conductivity fall mainly into three categories : i) The Green-Kubo (GK) method[22] provides an estimate of the thermal transport coefficient via the autocorrelation function of instantaneous heat fluxes which are straightforwardly computed in the course of an NVE (i.e., constant number of particles N, volume V and energy E) trajectory; ii) the "Non-Equilibrium Molecular Dynamics" or NEMD requires that a complete stationary state is established upon application of a temperature gradient to calculate the lattice thermal conductivity of a microcanonically (NVE) aged system; iii) the "approach-to-equilibrium molecular dynamics" (AEMD) deduce the lattice thermal conductivity from the spontaneous decay of a "step-like" (AEMD)[23,24] or "sinusoidal" (SAEMD)[25] temperature gradient toward zero over an NVE run.

A numerical comparison of the performances of these three methodologies is available in the Literature in the case of bulk crystalline silicon (c-Si) which is a prototypical system used to benchmark different MD-based methodologies; in contrast, such a comparison has not been done so far for organic semiconductors. As shown by Melis et al.,[23] the simulation time needed to obtain a well-converged thermal conductivity value for a c-Si sample consisting of 180 000 atoms, using AEMD, is about 200 ps, which corresponds to 2×10^5 simulation steps (by considering a time step of 1 fs). On the other hand, as highlighted by He et al.,[26] such a simulation time drastically increases in the case of GK and NEMD simulations. In detail, using GK on a system containing only 1728 atoms, a total simulation time as long as about 1 ns (10^6 simulation steps) is needed to estimate the c-Si thermal conductivity. Using NEMD, a total time of about 2 ns (2×10^6 simulation steps) is required to reach convergence on a system containing 11 520 atoms. Noteworthily, Giri, et al.[27] applied the classical Green-Kubo and non-equilibrium MD approaches with the polymer consistent force field (PCFF) to derive the lattice thermal conductivity of C_{60} and PCBM derivatives. However, the authors did not really discuss the benefits and limitations of the two different computational tools. In an earlier work, Shi et al.[28] investigated the thermal conductivity of some 2,7-dialkyl[1]benzothieno[3,2-b][1]-benzothiophene (Cn-BTBT-Cn) derivatives using the NEMD method. Nevertheless, they did not pay attention to the thermal transport along the stacking direction, most probably because the layered herringbone (LHB) arrangement is known to promote a two-dimensional (2D) charge transport owing to the very small electronic coupling between molecules lying in adjacent layers.[18,29,30] Interestingly, some of their other theoretical studies dedicated to the thermal conduction also ended up with the conclusion that heat transport was slightly anisotropic in organic small-molecular crystals such as pentacene[31] or phthalocyanine.[32]

In this context, we conduct here a comprehensive comparison of the Green-Kubo, non-equilibrium, and approach-to-equilibrium MD methods to estimate the lattice thermal conductivity in a single crystal made of terthiophene (hereafter

abbreviated 3T). The selection of this small molecule organic semiconductor as a prototype system is purely pragmatic, as 3T has the main advantage of having a quite simple chemical structure and a well-defined X-ray structure.[33] In addition, 3T derivatives (such as dihexylterthiophene) are potential candidates for the elaboration of efficient opto-electronic devices;[34] short thiophenic segments are also frequently encountered in many state-of-the-art (co)polymers used in the field of organic electronics. This paper is organized as follows: after this general introduction, the different MD-based methodologies employed for the description of thermal properties in 3T systems will be succinctly, yet comprehensively, exposed in Section 2. In Section 3, the thermal conductivities obtained from GK, NEMD, and AEMD results will be critically discussed. Finally, we will briefly summarize our main findings in Section 4. For the rest of the manuscript, we will refer to the phononic component of the heat transport simply as the "thermal conductivity," thereby deliberately disregarding contributions from electrons to the heat conduction. As predicted by the molecular Wiedemann-Franz law,[35] the electronic component of the thermal conductivity in weakly or undoped organic semiconductors is several orders of magnitude lower than their lattice counterpart,[36] whose values lie in the range of 10^{-2} –10^{0} W m^{-1} K^{-1}.[37]

2. Atomistic Simulation Methods

2.1. MD Simulation Details

Before applying the Green-Kubo, approach-to-equilibrium or non-equilibrium MD techniques, all simulation boxes were initially equilibrated through the following procedure. Samples have first been minimized with the volume of the experimental crystalline unit cell kept fixed and were then geometrically optimized by freely relaxing lattice parameters. These two steps were achieved by employing the conjugate gradient algorithm with a 10^{-8} and 10^{-8} kcal mol^{-1} Å^{-1} energy and force tolerance, respectively. Thereafter, the MD simulations have been successively conducted in the canonical (NVT) ensemble and then in the isothermal-isobaric (NPT) ensemble for 1 ns at a temperature of 300 K and at a pressure of 1 atm. The chosen temperature and pressure are consistent with actual experimental conditions for measuring thermal conductivities. For the description of the non-bonded interactions, we use the Particle-Particle and Particle-Mesh (PPPM) method for van der Waals and electrostatic interactions, with the cut-off set at 10 and 12 Å for each type of interaction. The equations of motion have been integrated by the velocity Verlet algorithm with time steps as short as 1 fs; thermostatting and barostatting have been attained by using the Nosé-Hoover algorithm with a coupling parameter of 0.1 ps and 1 ps, respectively.

2.2. Equilibrium MD

The Green-Kubo (GK) method relies on Equilibrium Molecular Dynamics (EMD) simulations and makes use of both the fluctuation-dissipation theorem[38] and the linear response theory to directly access (off)-diagonal components of the second order lattice thermal conductivity tensor, $\kappa_{\alpha\beta}$. According to the GK formalism, this quantity can be expressed as the autocorrelation function of the heat current as:

$$\kappa_{\alpha\beta} = \frac{1}{k_B T^2 V} \int_0^{\tau} J_\alpha(0)\, J_\beta(t)\, dt \tag{1}$$

where, k_B, stands for the Boltzmann constant; V, the volume of the system T, the temperature; τ, the time correlation corresponding to a cut-off time beyond which numerical errors prevent a reliable prediction of the heat current autocorrelation function;[39] $J_i(0)$, the heat current; and $J_\alpha(0)J_\beta(t)$, the heat current autocorrelation function (HCACF). In LAMMPS simulations, computed "heat fluxes" J_i are expressed in energy × velocity units; their mathematical form will be detailed hereafter. These quantities are then divided by the volume of the system in the input file to finally obtain the units of a "real" flux, namely energy per unit area per unit time. Note that the angular bracket in Equation (1) denotes an ensemble average and that the upper limit of this time integral, known as the correlation length τ, should be high enough to ensure a proper convergence of the corresponding matricial elements. In essence, Equation (1) states that the thermal conductivity is related to how long it takes for the fluctuations of the heat current $J_i(t)$ to dissipate at equilibrium (i.e., until the fluctuations have completely lost the memory of their original values). Over the years, a fair number of merits and drawbacks have been addressed to the EMD technique. On the one hand, two critical points in estimating the thermal conductivity within the GK approach arise from: i) the harsh numerical convergence of the heat current autocorrelation functions; ii) the need for a physically rigorous description of instantaneous heat fluxes (see Section 3.2). On the other hand, the GK formalism is alternatively praised for having less severe effects associated to cell size compared to both AEMD and NEMD methods and for giving a simultaneous access to the full thermal transport tensor within the course of only one single simulation (see Section 3.2).

2.3. Non-Equilibrium MD

The second approach followed in this study is the NEMD protocol. In short, the main principle consists in applying an external stimulus on a system in order to get an estimate of the bulk thermal conductivity by Fourier's law. Up to date, many ways of inducing a sustained heat flow or thermal pulse to measure thermal transport properties have been reported in the Literature. In this current work, we implemented a NEMD method relying on the approach developed by Müller-Plathe.[40] Herein, the simulation cell is subdivided into multiple slabs of the same thickness while a constant heat flux is imposed by artificially swapping kinetic energies between two spaced regions of the simulation box (commonly referred to as hot and cold reservoirs). Once the temperature gradient has attained a non-equilibrium steady state, instantaneous temperatures collected for each single slab are averaged over a certain time window. By combining a linear regression through this set of data with the exactly known amplitude of the exchanged heat flux, the thermal conductivity can be ultimately estimated.

Contrarily to the EMD method previously described, the non-equilibrium MD approach benefits from a faster convergence of

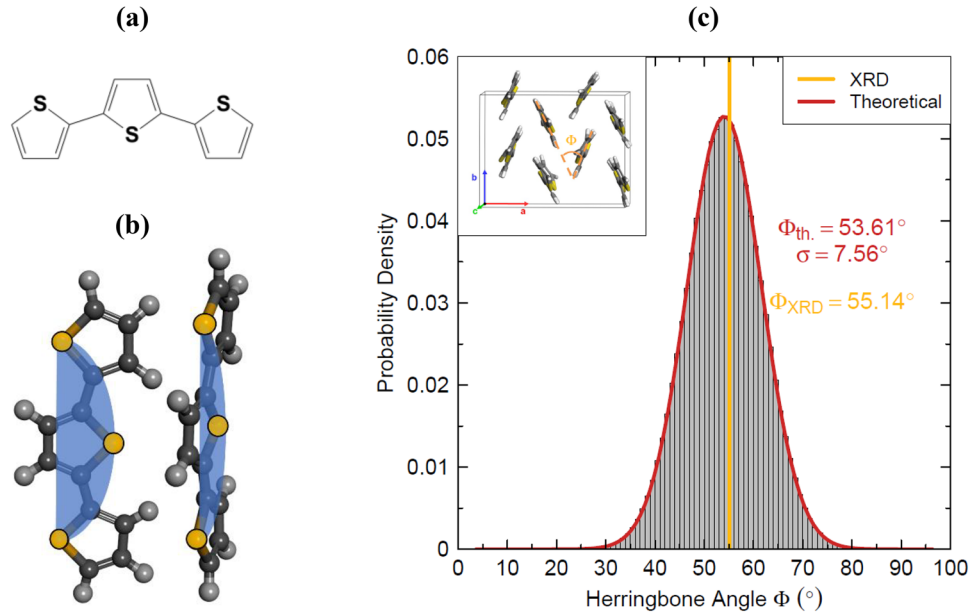

Figure 1. a) Molecular structure of 3T; b) Stick-and-ball representation of a pair of neighboring terthiophene molecules at 0 K. Carbon, hydrogen, and sulfur atoms are represented in black, grey, and orange, respectively. For sake of clarity, the molecular planes defined by the three sulfur atoms are represented in blue; c) Probability density in arbitrary units of the dynamical relative orientations of terthiophene molecules, as calculated from 50 snapshots extracted along a 1 ns NPT run for a 5 × 5 × 5 3T supercell. This distribution has been fitted by a Gaussian function (red); the average value $\Phi_{th.}$, the associated standard deviation σ, and the X-ray herringbone angle Φ_{XRD} (orange) are also reported. The herringbone arrangement of the 3T molecules in the *ab* plane is shown in the inset.

the temperature in comparison to that of the heat flux, hence generally requiring shorter time simulations to obtain properly converged results. However, one major pitfall associated with the NEMD algorithm is that larger simulation boxes are needed to achieve a size-independent thermal conductivity. To get rid of these finite size effects, an extrapolation procedure relying on the Matthiessen's rule is introduced, thus permitting to extract a quasi-length-free lattice thermal conductivity from the linear regression of $1/\kappa_i$ versus $1/L_i$ (with L_i the length of the box size along the *ith*-direction of heat propagation).

2.4. Approach-to-Equilibrium MD

The general scheme of AEMD consists in spatially delimiting the simulation box in two parts containing a similar amount of atoms. Once we have ensured that each compartment of the supercell has reached a thermal equilibrium after originally setting them at target temperatures $< T_1 >$ and $< T_2 >$, one can dissipate the generated thermal gradient and compute on the fly time-dependent difference in average temperatures, $\Delta T = < T_1 > - < T_2 >$ [K], between the two subsystems. The estimation of the lattice thermal conductivity can then be completed in an auxiliary post processing code (i.e., *R* studio) by fitting the previously monitored temperature profile with an accurate solution of the heat equation, $\frac{\partial T}{\partial t} = D\frac{\partial^2 T}{\partial i^2}$. The thermal diffusivity, $D = \kappa/\rho C_v$ [m^2 s^{-1}], is the only fitting parameter needed:

$$\Delta T = \langle T_1 \rangle - \langle T_2 \rangle = \sum_{n=1}^{\infty} C_n e^{-\alpha_n^2 Dt} \quad (2)$$

with n an integer and where the coefficients C_n are expressed as:

$$C_n = 8\left(T_1 - T_2\right)\frac{\left[\cos\left(\frac{\alpha_n L_i}{2}\right) - 1\right]^2}{\alpha_n^2 L_i^2} \quad (3)$$

with, L_i, the length of the simulation box along the specific direction of heat propagation and $\alpha_n = 2\pi n/L_i$. In the end, the thermal conductivity, κ [W m^{-1} K^{-1}], can be guessed from the above-mentioned relationship, as long as the mass density, ρ [kg m^{-3}], and the volumetric heat capacity, C_v [J kg^{-1} K^{-1}], of the system have been correctly estimated by means of classical MD simulations. A more detailed description of the theoretical procedures followed to assess the validity of the calculated ρ and C_v will be given in the related subsections.

3. Results and Discussion

3.1. Validation of the Force Field

The building of the terthiophene simulation boxes was based on the 3T structure reported in ref. [33] (**Figure 1**a) in which the unit cell of 3T is monoclinic (with a space group $P2_1/c$). The corresponding lattice parameters of the unit cell are: $a = 15.410$ Å, $b = 5.709$ Å, $c = 26.052$ Å, $\beta = 97.770°$. At room temperature, this organic compound is known to crystallize in a herringbone packing pattern, with a herringbone "edge-to-face" angle between vicinal molecules equal to 55.14° (i.e., the "low temperature" or *LT* polymorph).

Choosing an adequate empirical many-body potential is a very important criterion for gauging the reliability of classical

MD simulations. To be consistent with prior works reported in the Literature on similar organic systems,[28,31,41,42] all molecular mechanics and dynamics calculations were executed by the open-source classical molecular dynamics (MD) simulation code LAMMPS. The 3T molecule was modeled according to a specifically tailored version of the Optimized Potentials for Liquid Simulations All-Atoms (OPLS-AA) force field together with NBO-charges which were obtained via an NPA (Natural Population Analysis) using the Gaussian package with the PBE (Perdew-Burke-Ernzerhof) functional and the 6-311G(d,p) basis set. All default parameters in the bonding and non-bonding terms were taken from the LigParGen free server database; most of them appropriately reproduce X-ray bond lengths or carbon-sulfur-carbon X-ray angles (see Figure S2, Supporting Information). Nevertheless, particular attention should be addressed to mimic the torsion potential calculated at the Möller Plesset 2 level with a cc-pVTZ basis set (MP2/cc-pVTZ) between two adjacent thiophene units. A fitting procedure was then set up to capture as close as possible the minima and the barriers of the MP2 energy profile. As can be seen in Figure S1, Supporting Information, we truly determined a satisfactory combination of cosine terms to fit reasonably well this dihedral potential. When employed with the equilibration protocol outlined in Section 2.1 of this paper, such a finely tuned version of the OPLS-AA force field yields lattice parameters for a 3T supercell analogous to available experimental X-ray data (see Table S1, Supporting Information) and – no less importantly – it reliably models the layered herringbone packing of these organic molecules. This is evidenced by computing and comparing the herringbone angle Φ [°] between adjacent terthiophene molecules with corresponding X-ray measurements (Φ_{XRD} ≈55.14°).[33] To computationally evaluate the herringbone angle Φ, we defined and measured the angle enclosed by the normals to the molecular planes of two neighboring 3T molecules (see inset of Figure 1c). For ease of computation, we arbitrarily imposed these virtual planes to encompass the three sulfur atoms present in each molecular fragment (see Figure 1b). Such a procedure has been simultaneously repeated for all pairs of molecules belonging to a 5 × 5 × 5 supercell in 50 snapshots produced along a 1 ns NPT trajectory, thus allowing us to build some solid statistics. The fluctuations in Φ_{th} can be quantified by the standard deviation, σ [°], of its distribution. As reported in Figure 1c, the MD calculated herringbone angle Φ_{th} follows a Gaussian distribution, with an average value, $< \Phi_{th} >$ [°], and a standard deviation, σ [°], of 53.61° and 7.56°, respectively. Interestingly, the thermally induced molecular motions do not significantly affect the room temperature equilibrium crystal geometry since the standard deviation, σ [°], is quite small. Through the analysis of the resulting histogram, we also found that the average MD calculated herringbone angle matches fairly well its experimental X-ray counterpart.

After this equilibration setup, the density, ρ [g cm^{-3}], of the 3T bulk sample is estimated to be 1.49 g cm^{-3} at room temperature. The experimentally determined density of 3T is 1.50 g cm^{-3}, which is in good accordance with the density of our simulated structure. We consider this agreement with experimental densities satisfactory, which validates in turn the usage of the OPLS-AA force field for estimates of the thermal conductivity (see Section 2.4).

3.2. Equilibrium MD Results

3.2.1. Formulation of the Heat Flux

As already mentioned, the exact definition of heat current is of prime importance to accurately describe thermal transport coefficients using the Green-Kubo approach or any MD-based method that relies on the direct computation of instantaneous heat fluxes. In the regular version of the LAMMPS code, these heat currents are expressed in a virial stress formulation as follows:

$$\vec{J}\ (t) = \sum_i \varepsilon_i \vec{v}_i\ - \sum_i s_i \vec{v}_i \tag{4}$$

Herein, $\vec{v}_i$ is the velocity of atom i; ε_i is the total energy density associated with atom i and s_i is the per-atom stress component. For all m-body potentials in which the atom i is included, P_{mi}, the virial term is given by:

$$s_i = \frac{1}{V} \sum_{m=2}^{4} \sum_{\Phi \in P_{mi}} \frac{1}{m} \sum_{j \in \Phi} \vec{r}_j \vec{F}_{j\Phi} \tag{5}$$

where, $\vec{F}_{j\Phi}$, is the force on the atom j due to a specific potential Φ. However, this virial stress approximation has been recently challenged by several works,[43,44] demonstrating that the definition in Equation (5) applies only to two-body potentials (i.e., atomic crystals) and not to many-body potentials (i.e., molecular systems), as it was commonly accepted. In turn, Boone et al. developed a non-virial derivation of the instantaneous heat flux:

$$\vec{J}\ (t) = \sum_i \varepsilon_i \vec{v}_i\ + \frac{1}{V} \sum_{m=2}^{4} \sum_{\Phi \in P_m} \left(\frac{1}{m} \sum_{\{i,j\} \in (\Phi)^2} \left[\vec{r}_{ij} (\vec{F}_{i\Phi}.\vec{v}_i - \vec{F}_{j\Phi}.\vec{v}_j) \right] \right) \tag{6}$$

This corrected version of the instantaneous heat flux can be easily implemented in LAMMPS via the GitHub page (at https://github.com/wilmerlab/lammps) and is strictly equivalent to the previous virial expression when employed on a two-body potential system. They also pointed out that the error associated with the total heat flux calculation was found to be directly proportional to the amount of energy transferred via the angular (three-body; $m = 3$) and dihedral (four-body; $m = 4$) potential terms; this leads to an overestimation of heat fluxes and so, uncertainties in the computation of the thermal conductivity. In a concern for stringency, corrected and uncorrected LAMMPS virial stress heat fluxes will be subsequently and comparatively employed in this study, to consider how the choice can affect the final estimate of the thermal conductivity (see next subsection).

3.2.2. Convergence of HCACFs

Once the equilibration procedure described in the Methods section is achieved, we apply the Green-Kubo formalism to systems described using periodic boundary conditions (PBC). As a quick reminder, the estimation of the thermal conductivity through Equation (1) necessarily requires the direct computation of instantaneous heat fluxes. To do so, heat currents were collected

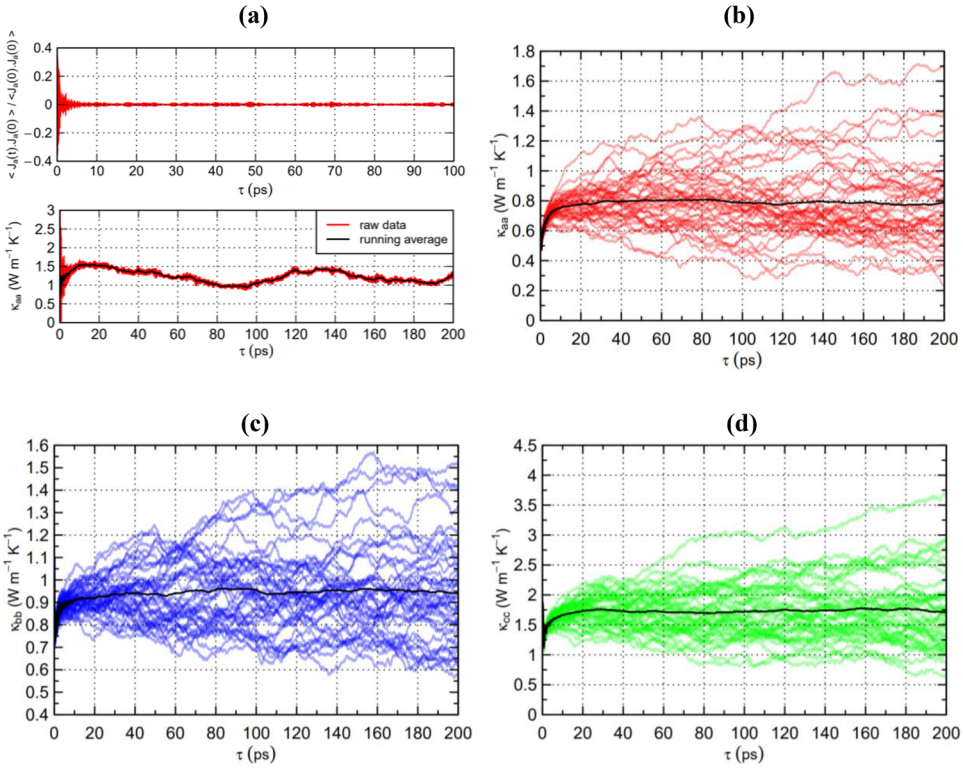

Figure 2. a) Top: convergence of the normalized autocorrelation function for the heat flux computed at room temperature along the crystallographic direction *a* in a 3T sample containing 1000 molecules (5 × 5 × 5 supercell) for a single trajectory using Equation (6); bottom: the corresponding thermal conductivity. b–d) Running thermal conductivities (κ) from the EMD method for a 3T sample containing 1000 molecules (5 × 5 × 5 supercell) using Equation (6) as a function of the correlation time τ along directions *a*, *b*, and *c*, respectively.

during an 2 ns NVE run (with a time step of 0.5 fs) and their autocorrelation was achieved by means of fast Fourier transforms within a post-processing step.[45] Note that heat current autocorrelation functions were sampled at every two time steps, to find a compromise between a better accuracy of the correlation integral and a reasonable amount of computational data to treat. For our materials, we define the volume, V [Å^3], from the cell parameters averaged over the last 500 ps of the NPT trajectory.

FFigure 2a portrays the resulting normalized heat current autocorrelation function and the corresponding thermal conductivity as a function of the correlation length on a 5 × 5 × 5 supercell, using Equation (6) for heat flux computations. Based on these results, it is clear that this above-described computational scheme is not suitable for achieving well-converged thermal conductivities due to the noise in the tail of the heat current autocorrelation functions. The convergence period is thus not long enough to deduce any reliable thermal conductivity values. To overcome this issue, a somewhat rough but convenient method has been developed alternatively by McGaughey et al.[46] and applied successfully to a wide range of materials, such as metal oxides[47] or 2D organic materials.[48] This procedure consists in performing parallel NVE simulations (differentiated by random initial velocities) and then performing a running average of the integral of the corresponding HCACFs by overlapping blocks of a few thousand steps (typically, 5000). The present procedure allows to smooth out short-term fluctuations in HCACF integral without affecting the overall trend. In theory, each of these starting configurations should yield the same thermal conductivity value, provided that the selected correlation window, τ, as well as the total simulation time for sampling heat fluxes are longer than the total lifetime of fluctuations in the equilibrium state of the system. However, such a way of proceeding would largely exceed available computational resources and then rapidly become infeasible for the study of realistic systems. In this context, they suggested to average the set of data obtained from the various replicas and predict the final thermal conductivity as soon as a convergence region is eventually identified. In this prospect, it is shown in Figure 2b–d that running averaged κ_{ii} (black solid lines) converges well in the range of 150 to 200 ps. 40 mean values were thus extracted in this range to access a representative mean value and associated standard statistical errors. As a result, it is found that even though the thermal conductivity might not independently converge for each propagation direction (red, blue, and green curves), a global convergence of the average thermal conductivity can be ultimately achieved (black curves).

Using this computational setup, we obtain thermal conductivities of κ_{aa} = 0.78 ± 0.04 W m^{-1} K^{-1}, κ_{bb} = 0.95 ± 0.04 W m^{-1} K^{-1} and κ_{cc} = 1.75 ± 0.09 W m^{-1} K^{-1} along the crystallographic directions *a*, *b*, and *c* using Equation (6). The corresponding values are κ_{aa} = 0.88 ± 0.06 W m^{-1} K^{-1}, κ_{bb} = 0.75 ± 0.03 W m^{-1} K^{-1} and κ_{cc} = 1.30 ± 0.07 W m^{-1} K^{-1} using Equation (4), respectively. Note that associated error bars were calculated as the standard deviation divided by the square root of the number of independent runs. The corresponding thermal conductivities

along directions *a*, *b*, and *c* employing the regular version of the LAMMPS code have been plotted in Figure S3, Supporting Information. For ease of comparison between values deduced from various protocol methods and along different crystallographic directions, we rely on the concept of anisotropic thermal conductivity ratio, κ_i/κ_j. Hence, the thermal conductivity ratios *a*/*b*, *c*/*a*, and *c*/*b* are 0.82, 2.24, and 1.84 using Equation (6) and 1.17, 1.47, and 1.73 using Equation (4); respectively. Surprisingly, it appears that both formulations of the instantaneous heat flux yield relatively similar results only along the *a*–axis while the GK values of κ_{bb} and κ_{cc} are about 27% smaller and 35% higher using Equation (6) with respect to those obtained from Equation (4). These discrepancies between values predicted along directions *b* and *c* are particularly challenging to explain since no direct correlation can be expected between a truncated estimation of heat fluxes due to an unphysical definition of $J(t)$ and the corresponding thermal conductivity predicted. Moreover, things are made more complicated by the fact that the statistical approach followed in this section might possibly hinder errors made in each trajectory, therefore attenuating greatly the impact of the exact formulation of the heat flux on final estimates of κ. Hence, the relative agreement between predictions along the *a*–axis could be the result of error cancellations. Concerning the anisotropic thermal conductivity, a direct comparison between the two sets of data indicates a quite pronounced anisotropy of the thermal transport with both the virial and non-virial formulations of $J(t)$; this is coherent with the predictions made with the two other out-of-equilibrium methods (see Sections 3.3 and 3.4). Finally, it should be stressed that if the methodology proposed by McGaughey actually offers the promise of providing properly converged results regardless of the formulation of the instantaneous heat flux considered, this protocol still remains very computationally demanding in comparison to both AEMD and NEMD methods (see Sections 3.3 and 3.4).

3.2.3. Size Effect

In order to eradicate size artifacts that are likely to affect the prediction of the thermal conductivity, we ran test cases at room temperature on 3T supercells of various sizes. We rely once again on 40 independent trajectories and 2 ns long simulations (with a time step of 0.5 fs) for each cell size. Within the Green-Kubo approach, the simulation results usually exhibit a much weaker dependence on size compared to both NEMD and AEMD methods. As evidenced on **Figure 3**, calculated κ of 3T supercells for samples ranging from 216 to 1000 molecules are modified by less than 8% along each of their three crystallographic directions. Indeed, the very few examples reported so far in the Literature achieve size-independent thermal conductivities by applying the GK formalism on simulation boxes usually consisting of less than a few hundreds of molecules.[27,49]

The most likely reason for this observation is that the evaluation of κ using the GK method only requires a sufficiently complete sampling of the phonon population dominating heat conduction. Consequently, the dimension of simulation boxes has to be large enough to ensure a reliable sampling of the phonons, thereby allowing for a converged prediction of thermal conductivities with increasing size. Interestingly, such a length independence in the GK framework is typically observed with simulation cells comparatively much smaller than those employed in the other two sets of classical approaches, hence considerably reducing the computational cost required for the estimate of κ. On the other hand, this apparent saving of computational resources is largely counterbalanced by the need to treat several dozens of independent samples to get a converged value of κ with a low uncertainty, as has been pointed out in the previous subsection. This ultimately makes this method numerically challenging to apply.

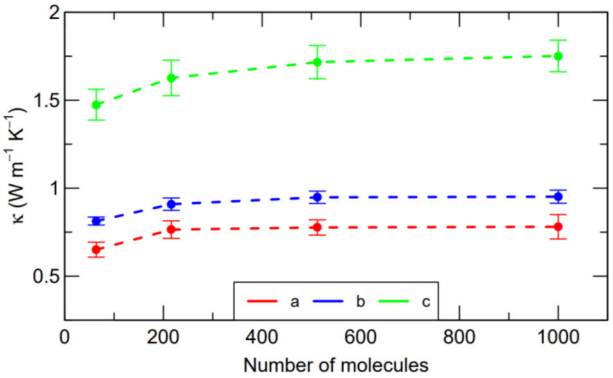

Figure 3. Room temperature thermal conductivity in 3T estimated by EMD, as a function of the number of molecules contained in periodically repeated 2 × 2 × 2, 3 × 3 × 3, 4 × 4 × 4 and 5 × 5 × 5 supercells along the crystallographic directions *a* (red), *b* (blue) and *c* (green). Each point is averaged over 40 independent simulations which were differentiated by random initial velocities. The time window selected for the averaging is between correlation time of 150 and 200 ps.

3.2.4. Off-Diagonal Elements of the Thermal Conductivity Tensor

Taking advantage of the Green-Kubo formalism, we calculated next the off-diagonal components of the thermal conductivity tensor via cross-correlations of HCACFs. From the results reported in Figure S4, Supporting Information, it is clearly observed that the diagonal elements of the thermal conductivity are main contributors to the total heat transport in 3T crystals since the off-diagonal thermal conductivities are negligible, with associated values close to zero or slightly negative. In details, we calculated κ_{ab} = 0.043 W m^{-1} K^{-1}, κ_{ac} = −0.022 W m^{-1} K^{-1} and κ_{bc} = −0.028 W m^{-1} K^{-1} using Equation (6). The Green-Kubo method has the advantage over both the AEMD and NEMD protocols that it gives access to the full thermal conductivity tensor within the course of one single trajectory. On the other hand, such an ability has a limited interest in the specific case of 3T crystals whose heat conduction appears to be largely dominated by κ_{aa}, κ_{bb}, and κ_{cc}.

3.3. Non-Equilibrium MD Results

We now turned to the investigation of the thermal transport in 3T systems by means of a NEMD approach. For this prospect, the chosen simulation sizes consisted of 16 to 64 unit cells for the directions *a* and *b*, and from 5 to 44 unit cells for the direction *c*, respectively. After running convergence test cases, their

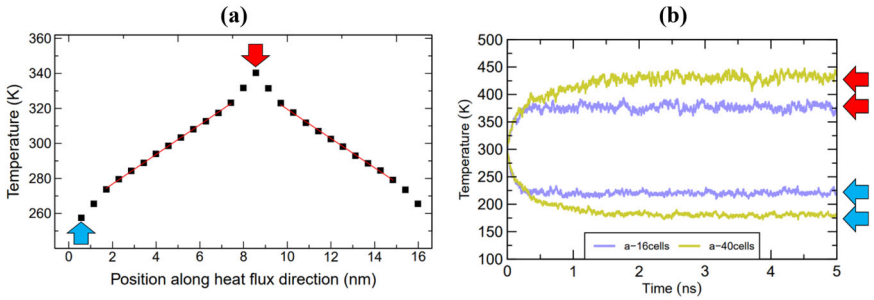

Figure 4. a) Induced temperature profile along the applied heat flux direction for a *b*-elongated supercell. The red and blue arrows denote the heat source and heat sink, respectively; b) Temperature evolution with time for both heat sink and heat source of two *a*-elongated supercells with N_a set to 16- (lavender lines) and 40-unit cells (mustard lines), respectively. Note that kinetic energies were swapped every 250 fs in both cases.

lateral sections were eventually built with periodic boundaries using 3 × 2, 2 × 2 and 2 × 4 3T supercells to mimic an infinitely large cross-section when the thermal conductivity was calculated along the directions *a*, *b*, and *c* in our all simulations, respectively. Following the equilibration procedure detailed previously in Section 2.1, systems were analyzed within the microcanonical ensemble (NVE) for 500 ps. The time step for all MD simulations is still fixed to 1 fs. Thereafter, NEMD simulations were conducted under NVE for 5 to 6 ns. In practice, supercells were consequently subdivided into *N* multiple bins parallel to the box face along the heat transport direction. We draw attention to the fact that in theoretical works previously reported,[27,31,32,50] this parameter was arbitrarily set to $N = 20$ or $N = 30$. In this study, we decided to systematically adapt the number of slabs *N* in each specific system in a such way that all slabs within a supercell enlarged in a given direction of heat propagation contain approximately an equal fraction of molecules (i.e., $N = 10$ for a 10 × 3 × 2 supercell, $N = 16$ for a 16 × 3 × 2 supercell, etc.).

As sketched in the inset of Figure 5, the middle region (red arrow) and an outermost slab (blue arrow) are set as the heat source and heat sink, respectively. Afterward, an initial heat flux was imposed via the Müller-Plathe algorithm by exchanging atomic kinetic energies every 250 time steps between heat and cold reservoirs in order to create and then maintain a sustainable temperature gradient throughout the whole simulation box (see **Figure 4**b). The selection of this specific value is directly based on benchmark calculations performed on a medium-size supercell elongated along the *a*–axis and for which the influence of the velocity swapping on the estimate of κ has been carefully investigated, see Table S2, Supporting Information. What is astonishing in the analysis of these data is that the linear response theory holds, regardless of the intensity of imposed heat fluxes. Hence, these results indicate that computed thermal conductivities are negligibly impacted by the rate in the velocity swapping, with thermal conductivity values remaining nearly constant even for heat fluxes on the order of $\approx 10^{11}$ W m^{-1}.

For all NEMD calculations on 3T systems, the generated steady thermal pulses lied in a range of 100–250 K, 50–100 K, and 100–200 K for *a*-, *b*- and *c*-elongated supercells, respectively. Finally, the Fourier's heat law is used to further extract thermal conductivity values from NEMD simulations, using the following expression:

$$\vec{J} = -\kappa \nabla T \tag{7}$$

Figure 4a displays a resulting steady state temperature profile for a *b*-elongated supercell of intermediate size; this example is fully representative of the other crystal orientations and simulation cell lengths under study. It is found that deviations from linearity arise in slabs acting as heat source and heat sink. In addition, these nonlinear effects become even more pronounced when the induced thermal gradient increases (i.e., when increasing simulation box length, L_i), as shown in Figure S5, Supporting Information. As suggested by D. Wang et al.,[31] these artifacts in temperature profiles can be partially attributed to unphysical exchanges of momentum between hot and cold reservoirs. To reduce statistical errors in the estimate of κ, we will exclude in the following points in the hot and cold slabs from the slope of a least-square fit of $T(t)$ versus distance (see the red solid line in Figure 4a).

It is worth noting that the total production run has been adapted based on the size of systems studied. This methodological choice is justified by Figure 4b, in which the temperature evolution with time of the heat source and heat sink are represented for two *a*-elongated supercells with small- and long-size lengths. These curves reveal that the induced thermal offset $\Delta T(t)$ is directly proportional to the corresponding simulation cell dimension, L_a. Subsequently, the increasing rate of $\Delta T(t)$ gets slower while increasing the cell size along which the thermal conductivity is calculated for a given velocity swapping. More precisely, a constant thermal gradient $\Delta T(t) \approx 100$ K is attained in less than 0.5 ns for a supercell elongated 16 times along direction *a* while almost 2 ns is required for achieving a steady $\Delta T(t) \approx 250$ K in a 40-unit cell system. Accordingly, the total simulation time in all NEMD simulations lasts from 5 to 6 ns; the system is set out of equilibrium within the first 1 or 2 ns and the thermal conductivity is then calculated during the remaining 4 ns. To estimate the associated standard deviations (i.e., error bars of dots in **Figure 5** and Figure S6, Supporting Information), the last 4 ns production run was split into 4 independent time blocks, with each block corresponding to a 1 ns trajectory. Then, the corresponding thermal conductivity was estimated for each portion *i* and the standard deviations σ^2 were deduced from their averaging.

In contrast to the EMD method, such a manner of accounting statistical errors in the estimate of the thermal conductivity via the non-equilibrium MD approach is far less computationally prohibitive than producing the mean of κ over several 6 ns-long independent trajectories. Finally, one common artifact usually faced when performing NEMD simulations on

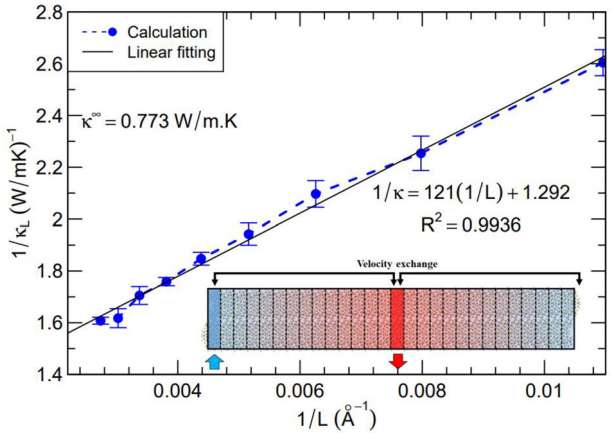

Figure 5. The calculated inverse of thermal conductivity $1/\kappa_b$ with different sizes L_b, and linear extrapolation of $1/\kappa_b$ versus $1/L_b$ using NEMD simulations. Sketch of the Müller-Plathe algorithm is shown in inset (as inspired by the ref. [42]).

non-orthorhombic supercells is that the heat propagates in a direction perpendicular to the cell wall rather than along the real crystal directions *a*, *b*, and *c*. Transposed to our 3T system, this implies that heat fluxes are imposed along directions *a*, *b*, and *c** instead of *c* due to the monoclinic character of its unit cell ($\beta = 97.770°$). In order to provide a consistent comparison with simulation data obtained from both GK and AEMD methods, extra care has been exercised to properly realign lattice vectors of *c*-elongated supercells via the Materials Studio software in such a way that their *c*–axis corresponds to the actual thermal conduction direction, as shown in the inset of Figure S6, Supporting Information. "Infinite-length" thermal conductivity values are obtained from the linear fit of data collected along each crystallographic direction (see Figure 5 for axis *b*) according to a Matthiessen-like relationship: $1/\kappa_i = (1/\kappa_\infty).(1 + \lambda/L_i)$. These are found to be: $\kappa_a = 1.01 \pm 0.03$ W m^{-1} K^{-1}, $\kappa_b = 0.77 \pm 0.02$ W m^{-1} K^{-1} and $\kappa_c = 1.69 \pm 0.06$ W m^{-1} K^{-1}, respectively. The corresponding thermal anisotropy indices *a*/*b*, *c*/*a*, and *c*/*b* are 1.31, 1.67, and 2.19, respectively.

Unsurprisingly, thermal conductivities exhibit a stronger size dependence in comparison with the GK approach. Indeed, such trends are expected since phonons with longer MFPs are believed to contribute more significantly to the conductive heat transport when increasing cell lengths while phonon boundary scatterings are reduced. Similarly to our previous predictions based on the Green-Kubo method, we again highlight an anisotropy in the thermal conductivity in 3T crystals, with the highest thermal conductivity value predicted along the interlayer axis with respect to those in-plane. Such a directional dependence in κ can be attributed to the structural anisotropy of the layered herringbone packing crystal. A comparison with results obtained from the GK method using Equation (4) clearly indicates that thermal conductivities along the three principal axes are higher with NEMD, although the same empirical many-body potential was employed in both cases. Compared to the virial GK formula, the non-equilibrium MD approach overestimates κ by about ≈15% and ≈30% along the *a*– and *c*–axes while a quantitative agreement is observed only in the direction *b*. In principle, these two approaches are supposed to give similar results. This discrepancy can be convincingly rationalized by the fact that contrarily to the Green-Kubo formalism, the NEMD method provides the upper limit of thermal conductivity for the bulk since extrapolated predictions refer to an infinitely long sample in a purely diffusive regime with perfect crystallinity. Hence, unsuppressed finite size effects in Green-Kubo method could be at the origin of slight underestimations of κ with respect to NEMD. Nevertheless, this argument has a limitation: our previous simulations based on the non-virial GK formula show that the thermal conductivity along the *b*–axis is on average 27% larger than that computed by Fourier's law (see Section 3.1); this overestimation is not exactly in line with rules dictated by finite size effect theories. In addition, most of the theoretical methodologies implemented in this work have predicted a thermal conductivity ratio *a*/*b* larger than the unity (see the central part of **Table 1**) while this trend was not observed solely with the non-virial GK formula. In this regard, it is our feeling that much caution has to be exercised when considering results obtained from Equation (6) and that data provided by the virial GK formula might be more meaningful for a relevant comparison with the other two computational tools.

3.4. Approach-to-Equilibrium MD Results

3.4.1. Heat Capacity

As mentioned before, trustworthy estimates of the thermal conductivity within the approach-to-equilibrium MD approach implies to correctly predict the mass density ρ and the volumetric heat capacity C_v of the system. The heat capacity, C_v [J mol^{-1} K^{-1}], was calculated for the terthiophene (3T) following the methodology proposed by McGaughey and Kaviany.[46] In detail, the total energy E of a 5 × 5 × 5 3T supercell is computed at T = 288, 293, 298, 303, and 308 K in a 1 ns-long microcanonical MD run and the results are averaged over the last 50 ps using 10 different initial configurations as starting points. According to classical thermodynamics, the heat capacity C_v can be deduced as the first derivative of the total energy E with respect to the temperature T at constant volume V (see Figure S7, Supporting Information):

$$C_v = \left.\frac{\partial E}{\partial T}\right|_V \tag{8}$$

The linear fitting of $E(T)$ gives a specific heat equal to C_v = 25.049 J mol^{-1} K^{-1} at room temperature, which is in good agreement with the value predicted by the Dulong-Petit theory (C_v^{DP} ≈ 24.942 J mol^{-1} K^{-1}), stating that the heat capacity, C_v, of any material is equal to *3R*, with *R* the perfect gas constant. For ease of computation, this basic model, built upon the hypothesis that atomic motions can be treated as a collection of classical harmonic oscillators vibrating around their equilibrium positions, will be assumed as a reasonable approximation to the real quantum behavior and thus employed in this study.

3.4.2. Finite Size Effects and Extrapolation Rule

In MD simulations, it is well known that the prediction of the thermal conductivity depends on the actual length L_i of the

Table 1. Left: Bulk thermal conductivities, $\kappa_{i,\infty}$, along the three main crystallographic directions *a*, *b*, and *c* for 3T systems using GK with two different formulations of instantaneous heat flux, NEMD, and AEMD using two different analytical fitting models; middle: associated thermal conductivity ratios, $\kappa_{i,\infty}/\kappa_{j,\infty}$; Right: Corresponding computational costs for each approach..

	$\kappa_{i,\infty}$ *)			$\kappa_{i,\infty}/\kappa_{j,\infty}$			Computational cost#)		
Method	*a*	*b*	*c*	*a/b*	*c/a*	*c/b*	*a*	*b*	*c*
GK using Equation (4)	0.88	0.75	1.30	1.17	1.47	1.73	53.3	53.3	53.3
GK using Equation (6)	0.78	0.95	1.75	0.82	2.24	1.84	53.3	53.3	53.3
NEMD	1.01	0.77	1.69	1.31	1.67	2.19	51.0	51.0	53.0
AEMD using Equation (9)	1.06	0.81	1.97	1.29	1.87	2.41	23.0	24.0	19.5
AEMD using Equation (10)	1.14	0.79	2.06	1.44	1.81	2.61	23.0	24.0	19.5

*) Thermal conductivities are given in W m^{-1} K^{-1}; #) Computational cost is given in mega time steps.

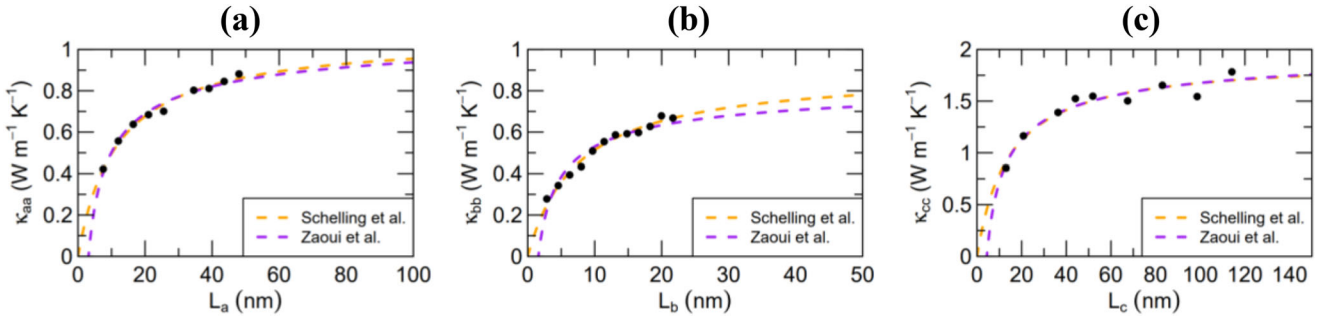

Figure 6. Thermal conductivity (κ) of 3T systems computed along the crystallographic directions *a*, *b*, and *c* at room temperature, as a function of the length of the periodic slab (L_i) using approach-to-equilibrium molecular dynamics (AEMD). Orange and purple dotted lines represent a fit to Equations (9) and (10), respectively.

selected simulation cells, especially when sample dimensions are smaller than the average phonon MFP governing heat transport. These finite size effects can significantly vary depending on the kind of MD-based methods chosen for computing κ.

Within the AEMD approach, finite size effects are believed to strongly affect the evaluation of the bulk thermal conductivity. Over the recent years, several theoretical models have been developed to take them into account. As for the non-equilibrium MD approach, a Matthiessen-like relationship based on the kinetic theory definition of the heat transport[51] has first been used to extrapolate a thermal conductivity at the infinite limit κ_∞ from a set of $\kappa(L_i)$ computed for several samples of length L_i, as:

$$\kappa\ (L_i) = \kappa_\infty / \left(1 + \frac{\lambda}{L_i}\right) \tag{9}$$

where λ has the dimension of a length. In this mathematical fitting function, a L_i-dependence is explicitly introduced via an additional term accounting for scattering processes due to the presence of system/thermal reservoir boundaries, the latter playing the role of diffusive interfaces. Until very recently, this formulation developed by Schelling et al. (as well as the one very similar proposed by Sellan et al.[52]) was supposed to be a "cardinal" rule to suppress size effects while estimating the thermal conductivity by means of out-of-equilibrium MD runs.

However, in the AEMD approach, the effective size effect cannot be physically attributed to phonon boundary scatterings since no other sources of scattering except the phonon-phonon terms are supposedly present. Alternatively, Zaoui et al.[53] developed an analytical fitting model in which acoustic phonons are regarded as main carriers of heat at the microscopic level:

$$\kappa\ (L_i) = \kappa_\infty \left(1 - \sqrt{\frac{\Lambda}{L_i}}\right) \tag{10}$$

with Λ, another parameter also expressed in length unit. As can be seen on **Figure 6**, extrapolation to $1/L_i \approx 0$ using these two fitting procedures yields very similar results, despite the fact of having been derived under different assumptions. In details, we obtained thermal conductivities $\kappa_a = 1.06 \pm 0.02$ W m^{-1} K^{-1}, $\kappa_b = 0.81 \pm 0.03$ W m^{-1} K^{-1} and $\kappa_c = 1.97 \pm 0.08$ W m^{-1} K^{-1} using Equation (9) and $\kappa_a = 1.14 \pm 0.02$ W m^{-1} K^{-1}, $\kappa_b = 0.79 \pm 0.03$ W m^{-1} K^{-1} and $\kappa_c = 2.06 \pm 0.07$ W m^{-1} K^{-1} using Equation (10). These observations are in good accordance with those reported in one earlier work[25] in which Puligheddu et al. compared these two fitting models when applying the sinusoidal AEMD approach for the study of thermal transport on a prototypical system of

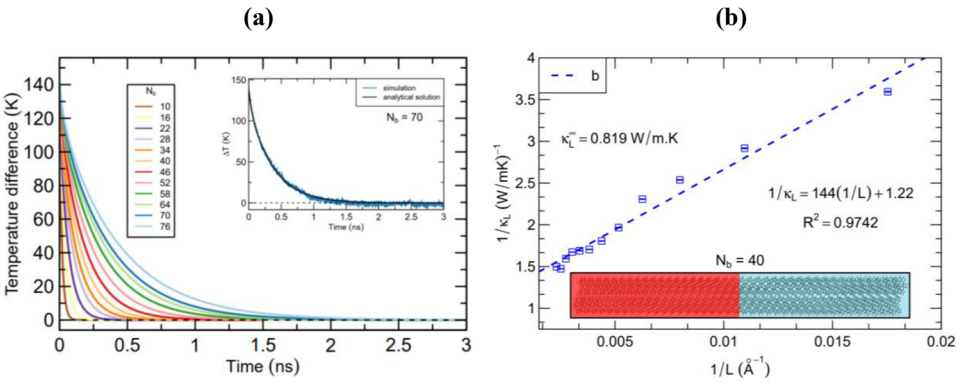

Figure 7. a) The average temperature difference $\Delta T(t)$ as simulation time progresses, with increasing simulation box size L_b, fitted to an exponential function. The inset shows ΔT as a function of simulation time for real values (blue-colored line) and the fitting line (black-colored smooth line) for the case of $N_b = 70$ unit cells (≈40 nm); b) The calculated inverse of thermal conductivity $1/\kappa_b$ with different sizes L_b, and linear extrapolation of $1/\kappa_b$ versus $1/L_b$ using AEMD simulations.

c-MgO. Besides, it is worth noticing that such a comparison has not been done so far for organic semiconductors. For sake of consistency, we will thus employ the same extrapolation procedure (i.e., the "Schelling model") to fit and compare results deduced from both NEMD and AEMD methods in our theoretical benchmark.

3.4.3. Critical Comparison of MD-Based Results

Following the equilibration protocol described in detail in Section 2.1, we applied the approach-to-equilibrium MD methodology on 3T systems. First, an initial "step-like" thermal pulse between the two halves of the simulation cells ΔT_0 was set at 100 K for all cell sizes L_a and L_c, and at 150 K for simulation boxes of cell size L_b. Such huge thermal offsets should guarantee a better precision on the fitting time, with decay signals clearly distinguishable from remaining thermal noises at equilibrium.[53] Practically, the chosen systems were split into two regions which were subsequently thermalized at different temperatures during two consecutive NVT simulations of 250 ps each. Afterward, this initial constraint is removed through a NVE run to let the system free to reach thermal equilibrium ($\Delta T_{t>>0} \approx 0$ K). It should be noted that the duration of this last simulation is specifically adapted to the length of the system. From the check of convergence with respect to the cross-section, S_{ij}, of samples used (see Figure S8, Supporting Information), we have observed that the variation of thermal conductivity is around 7.4% for S_{bc} ranging from 3 × 2 to 4 × 3 terthiophene supercells along *a*, around 2.6% for S_{ac} ranging from 2 × 2 to 3 × 3 unit cells along *b* and around 2.9% for S_{ab} ranging from 2 × 3 to 3 × 4 lattice units along *c*, respectively. Such slight variations indicate that κ is marginally affected by the change in corresponding cross-sections.[54] Based on the above benchmark, we chose to apply the approach-to-equilibrium MD methodology on supercells having a cross-section of 3 × 2 lattice units along the direction *a*, of 2 × 2 lattice units along the direction *b* and of 2 × 4 lattice units along the direction *c*, respectively. For each of the investigated directions, we took care to choose the length L_i for samples much longer than the corresponding cross-section of the supercells, in order to be certain of inducing a 1D heat transport along the desired *i*th–axis. In details, cell size L_i was varied from 10 to 64 lattice units with 7 intermediate points for the *a*–axis, from 10 to 76 lattice units with 10 intermediate points for the *b*–axis, and from 5 to 44 lattice units with 5 intermediate points for the *c*–axis, respectively.

Figure 7a displays the fitted time-decaying temperature differences $\Delta T(t)$ between the right and left parts of a collection of supercells elongated along the direction *b*. From the analysis of these curves, it appears that increasing the cell length L_b may substantially delay the dissipation of the thermal pulse while slightly enhancing the fitting accuracy. Still, it is found that the approach to thermal equilibrium occurs in a fast transient regime even for the largest systems under study, such as the 2 × 76 × 2 3T supercell whose ΔT has nearly fallen down to 0 K after only 1.5 ns. Interestingly, this remarkably reduces the computational cost with respect to the other GK and NEMD techniques.

Each dot in Figure 7b has been obtained by accurately fitting monitored $\Delta T(t)$ (blue line shown in the inset of Figure 7a) to an exponential function based on five terms (see Equation (2)), to give the thermal diffusivity *D* and finally the thermal conductivity $\kappa(L_b)$, provided that the volumetric heat capacity C_v and density of the system ρ have been properly defined. Note that a fitting function based on five terms appears to be the best compromise between reasonable computational time and sufficient accuracy for the estimation of the lattice thermal conductivity. It is worth noting that the use of Equation (2) as fitting mathematical function is supported by the curve plotted in the inset of Figure 7a where the transient to the equilibrium temperature is clearly exponential. Figure 7b shows the inverse of the calculated thermal conductivity as a function of the inverse of the super cell length L_b. Corresponding plots for the directions *a* and *c* can be examined in Figure S9, Supporting Information. Linearly extrapolating $\kappa(L_i)$ to the limit of $L_i \to \infty$ using Equation (9) yields thermal conductivities of $\kappa_a = 1.06 \pm 0.02$ W m^{-1} K^{-1}, $\kappa_b = 0.82 \pm 0.05$ W m^{-1} K^{-1} and $\kappa_c = 1.97 \pm 0.07$ W m^{-1} K^{-1}, and corresponding thermal anisotropy ratios of *a*/*b*, *a*/*c*, and *c*/*b* are 1.29, 1.87 and 2.41, respectively. Interestingly, these theoretical predictions are again very similar to the previous simulation data calculated using

the same OPLS-AA force field with both the Green-Kubo and non-equilibrium MD methods.

Accordingly, a detailed comparison of values collected from this set of computational tools clearly highlights an anisotropic thermal transport in terthiophene crystals, with thermal conductivities nearly two times higher along the direction *c* with respect to those along the *a*– and *b*–axes. However, the absence of corresponding experimental thermal conductivity measurements prevents at this stage a better evaluation of the level of accuracy for each of these MD-based methods. On the contrary, a meaningful overview of their computational performance is readily accessible. In the GK case, the slow convergence of heat fluxes implies to run MD with relatively long simulation times in order to suppress the noise in the tail of heat current autocorrelation functions. In addition, converged predictions based on the Green-Kubo formalism can only be achieved by averaging data obtained from a large panel of parallel independent runs (up to 40 trajectories), thereby increasing significantly the overall computational cost. When using the non-equilibrium MD formulation, the total simulation time required to obtain a reliable thermal conductivity value is related to i) the time needed to put the system out of the equilibrium by inducing a stable thermal gradient between its two extremities (ranging between 1 and 2 ns); ii) an additional time period (≈4 ns) to keep the system in this stationary state and to predict the thermal conductivity while making sure to reduce uncertainties in the determination of κ. In contrast to the other two methods, the AEMD approach makes use of the exponential decay of the initially imposed thermal offset to accurately evaluate the thermal conductivity on a much shorter time window (i.e., approximately within a few hundreds of picoseconds in most cases).

Taking advantage of this much cheaper computational burden, the AEMD approach will now be exploited to study the influence of temperature on the thermal transport in organic crystals.[42]

3.4.4. Temperature Dependence

To gain insight in the temperature dependence of the thermal conductivity of single crystals made of terthiophene, we applied here the approach-to-equilibrium MD protocol following a methodology proposed by Wang et al.[42] The selection of this method is justified by the previous benchmark in which we have demonstrated that the AEMD was the most suitable method in terms of both accuracy and computational workload to assess thermal conductivities in this organic prototypical system.

For each temperature, we have first equilibrated three different configurations which were initially obtained at selected temperature from an initialization with different atomic velocities following a Maxwell-Boltzmann distribution, as we did for the GK approach. Afterward, we calculated their corresponding average thermal conductivities and standard deviations, here ascribed as statistical errors. More precisely, the AEMD methodology was applied on a set of temperatures ranging from 100 K to 350 K with an interval of 50 K. It is worth mentioning that no quantum effects are expected to arise under these conditions since the selected target temperatures remain above the range of Debye temperature, θ_D [K], scarcely reported for organic materials (i.e., far below 100 K). For each direction of interest, the initially imposed

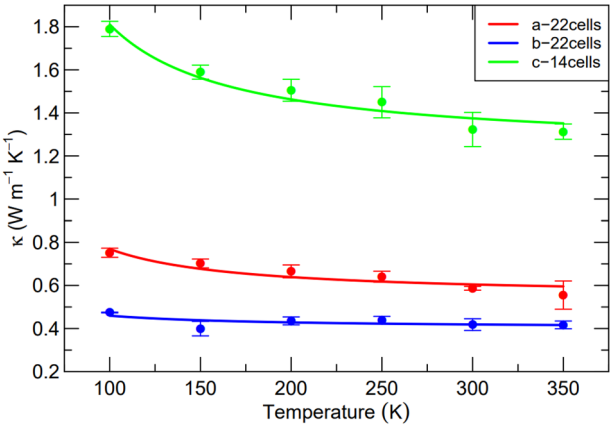

Figure 8. Temperature dependence of the thermal conductivity for 3T along *a*, *b*, and *c* directions. Solid lines represent fitting curves between κ and T based on the relation: $\kappa \propto 1/T$.

temperature gradients as well as the cross-sectional size of the simulation boxes were the same as that in the previous AEMD simulations performed at *RT*. These choices are motivated by making the assumption that the dependence of κ with both the cross-section and ΔT_0 changes marginally with temperature. To reduce the computational cost, we decided to carry out calculations on a single sample (displaying an "intermediate" length) per direction, namely: *a*-22 unit cells; *b*-22 unit cells; and *c*-14 unit cells. What actually matters the most in our opinion is to provide relative variations of κ with temperature rather than accurate "infinite-length" values since no experimental thermal conductivity of terthiophene is currently available for a direct comparison.

Figure 8 displays the thermal conductivity of terthiophene along the three crystallographic directions at different simulation temperatures. Similarly to the thermal transport previously studied at room temperature, the temperature effect on κ is also anisotropic, as suggested in Figure 8. In particular, our theoretical results show that the thermal conductivities of terthiophene along the directions *a* and *c* are reduced by ≈27% when the temperature rises from 100 K to 350 K. On the contrary, the thermal conductivities along the direction *b* remain nearly unchanged, with a decrease of only ≈11% through the whole temperature range. Such findings can be theoretically rationalized by introducing two supplementary physical quantities: phonon MFPs and phonon group velocities. Of notable interest is that the phonon MFPs, L_{MFP} [nm], can be extracted from the analytical equations associated with the extrapolation curves. Without dwelling on theoretical concepts that have been discussed in more details in one of our previous papers,[36] we simply mention here that such a deduction is made possible by combining the kinetic formulation of the thermal conductivity (namely, $\kappa = \frac{1}{3}\rho C_v \tau_{bulk}^2 L_{MFP}$, where τ_{bulk} [fs] is the bulk phonon relaxation time) with the decomposition of τ_{bulk} into separate terms due to the independence of the various scattering events arising in the system, as predicted by the Matthiessen's rule. The calculated average phonon MFPs along directions *a*, *b*, and *c* are 11.1, 5.9, and 8.0 nm for 3T at room temperature, while phonon group velocities yield an order $c > b > a$.

Based on these results, it is found that crystalline 3T exhibits longer average phonon MFPs along the directions *a* and *c* with respect to that along the direction *b* and a larger average phonon group velocity along the *c*–axis with respect to those along the *a*– and *b*–axes. As already described elsewhere in the Literature,[42,55] it is widely admitted that phonon-phonon Umklapp (*U*-) scattering becomes predominant as the temperature increases, hence presumably giving rise to a notable drop of the thermal conductivity following the relationship: $\kappa \propto 1/T$. In the *U*-process, two phonons with wavevectors K_1 and K_2 give rise to a new third phonon whose resulting wavevector K_3 is "folded back" by the reciprocal lattice vector *G*. Therefore, the energy is conserved in the *U*-process, but not the momentum: this means that the phonon–phonon Umklapp scattering directly contributes to the total thermal resistivity. When the temperature rises, phonon MFPs are expected to be reduced through *U*-processes but this effect is likely to impact less thermal transport along the direction *b* since both the MFP and the group velocity are already much shorter than those along the *a*– and *c*–axes. Moreover, the assumption of a predominant "Umklapp regime" in terthiophene crystals is supported by fitting our MD results with an expression based on the Callaway's model,[56] which assumes that $\kappa(T)$ decreases at higher temperatures according to $\kappa \propto T^{-1}$.

4. Conclusions

In summary, we have achieved a detailed comparative study of the classical GK, NEMD, and AEMD approaches with the all-atom version of the Optimized Potential for Liquid Simulations (OPLS-AA) force field for deriving the room temperature lattice thermal conductivity of crystalline 3T. Corresponding thermal conductivities and associated anisotropic coefficients deduced from the above set of computational tools are summarized in Table 1.

In order to consistently estimate and compare their computational performances, the total number of time steps required for estimating "infinite-length" thermal conductivity values by means of the GK, NEMD, and AEMD approaches have also been indicated on the right of Table 1. Note that this quantity has been divided by three in the specific case of the Green-Kubo formalism since all diagonal elements of the thermal conductivity are accessible from one single trajectory. Concerning the GK method, it is found that carrying out multiple independent trajectories for smaller time durations (≈2 ns) is more effective to get properly converged thermal conductivities than performing one single calculation for a very large number of time steps. It should be noted that this statement holds regardless of the definition of the heat flux considered. In more detail, using the non-virial formulation of $J(t)$, different trends are observed for the heat conduction with respect to those computed from both AEMD and NEMD approaches. Intriguingly, we showed that the non-virial definition of the heat flux overestimates the GK value of κ_b compared to Fourier's law, which appears to be odd with regular finite size effect theories. This coupled with a thermal conductivity ratio a/b unusually smaller than the unity raises doubts about the ability of Equation (6) to reliably estimate the thermal conductivity within the Green-Kubo method. In the Green-Kubo formalism, the entire lattice thermal conductivity tensor can be fully deduced from one single trajectory, unlike the NEMD and AEMD methods which necessitate several simulations in each direction to achieve the same result. However, our calculations revealed that off-diagonal contributions to the total conductive heat transport are clearly negligible, therefore diminishing substantially the relevance of such a feature over the other two out-of-equilibrium approaches.

A more satisfying agreement is achieved between NEMD and AEMD predictions, both for absolute and relative values. Nevertheless, the AEMD approach completely outperforms NEMD in terms of computational resources. This can be readily explained by the fact that the thermal conductivity is computed in a transient regime instead of a steady state within the AEMD, which is much less computationally prohibitive. Hence, typical simulation times to attain equilibrium are shorter by about a factor of 2 to 4, compared to those required by the NEMD method. In detail, using AEMD approach instead of NEMD, the total amount of computational resources required for achieving "infinite-length" thermal conductivity values is divided by a factor ranging between 2.1 and 2.7 (see the right part of Table 1). Last, the approach-to-equilibrium MD method can be almost seen as a "parameter-free" model whose implementation is very easy in comparison with other approaches such as Green-Kubo.

As a result of this benchmark, the approach-to-equilibrium MD method was then applied over a certain range of temperatures on 3T systems to further discuss the dependence of κ on factors other than crystal orientations. Strikingly, the temperature dependence of heat transport was also found to be anisotropic. To get a better understanding of the thermal effect on κ, phonon MFPs and phonon group velocities have been estimated in the three main directions of heat propagation. We established that thermal conductivity demonstrates an Umklapp scattering-dominated temperature evolution ($\kappa \propto T^{-1}$), which is consistent with previously reported data on similar organic compounds.[42]

Supporting Information

Supporting Information is available from the Wiley Online Library or from the author.

Acknowledgements

The authors acknowledge stimulating discussions with Prof. Luca Muccioli, Dr. Julien Idé, Prof. Zhigang Shuai, Dr. Dong Wang, Prof. J.L. Brédas, and Dr. V. Coropceanu. The work in the Laboratory for Chemistry of Novel Materials was supported by the Consortium des Équipements de Calcul Intensif (CÉCI), funded by the Fonds de la Recherche Scientifique de Belgique (F.R.S.-FNRS) under grant no. 2.5020.11. J.C. is an FNRS research director.

Conflict of Interest

The authors declare no conflict of interest.

Data Availability Statement

The data that support the findings of this study are available from the corresponding author upon reasonable request.

Keywords

approach-to-equilibrium molecular dynamics, Green-Kubo formalism, heat transport, non-equilibrium molecular dynamics, organic electronics

Received: December 5, 2022
Revised: February 15, 2023
Published online:

[1] G. Fugallo, L. Colombo, *Phys. Scr.* **2018**, *93*, 043002.
[2] B. Russ, A. Glaudell, J. J. Urban, M. L. Chabinyc, *Nat. Rev. Mater.* **2016**, *1*, 16050.
[3] S. Volz, J. Ordonez-Miranda, A. Shchepetov, M. Prunnila, J. Ahopelto, T. Pezeril, G. Vaudel, V. Gusev, P. Ruello, E. M. Weig, M. Schubert, M. Hettich, M. Grossman, T. Dekorsy, F. Alzina, B. Graczykowski, E. Chavez-Angel, J. Sebastian Reparaz, M. R. Wagner, C. M. Sotomayor-Torres, S. Xiong, S. Neogi, D. Donadio, *Eur. Phys. J. B* **2016**, *89*, 15.
[4] T. Vasileiadis, J. Varghese, V. Babacic, J. Gomis-Bresco, D. Navarro Urrios, B. Graczykowski, *J. Appl. Phys.* **2021**, *129*, 160901.
[5] Y. Khan, A. E. Ostfeld, C. M. Lochner, A. Pierre, A. C. Arias, *Adv. Mater.* **2016**, *28*, 4373.
[6] D. G. Cahill, *Rev. Sci. Instrum.* **1990**, *61*, 802.
[7] V. Chiloyan, L. Zeng, S. Huberman, A. A. Maznev, K. A. Nelson, G. Chen, *Phys. Rev. B* **2016**, *93*, 155201.
[8] L. Zeng, K. C. Collins, Y. Hu, M. N. Luckyanova, A. A. Maznev, S. Huberman, V. Chiloyan, J. Zhou, X. Huang, K. A. Nelson, G. Chen, *Sci. Rep.* **2015**, *5*, 17131.
[9] A. J. Minnich, J. A. Johnson, A. J. Schmidt, K. Esfarjani, M. S. Dresselhaus, K. A. Nelson, G. Chen, *Phys. Rev. Lett.* **2011**, *107*, 95901.
[10] P. Jiang, L. Lindsay, Y. K. Koh, *J. Appl. Phys.* **2016**, *119*, 245705.
[11] M. Omini, A. Sparavigna, *Phys. B* **1995**, *212*, 101.
[12] G. Fugallo, M. Lazzeri, L. Paulatto, F. Mauri, *Phys. Rev. B* **2013**, *88*, 45430.
[13] M. Puligheddu, Y. Xia, M. Chan, G. Galli, *Phys. Rev. Mater.* **2019**, *3*, 85401.
[14] R. Peierls, *Ann. Phys.* **1929**, *395*, 1055.
[15] F. Zhou, W. Nielson, Y. Xia, V. Ozoliņš, *Phys. Rev. Lett.* **2014**, *113*, 185501.
[16] S. Baroni, S. de Gironcoli, A. Dal Corso, P. Giannozzi, *Rev. Mod. Phys.* **2001**, *73*, 515.
[17] A. J. C. Ladd, B. Moran, W. G. Hoover, *Phys. Rev. B* **1986**, *34*, 5058.
[18] G. Schweicher, G. D. Avino, M. T. Ruggiero, D. J. Harkin, K. Broch, D. Venkateshvaran, G. Liu, A. Richard, C. Ruzié, J. Armstrong, A. R. Kennedy, K. Shankland, K. Takimiya, Y. H. Geerts, J. A. Zeitler, S. Fratini, H. Sirringhaus, *Adv. Mater.* **2019**, *31*, 1902407.
[19] N. Bedoya-Martínez, A. Giunchi, T. Salzillo, E. Venuti, R. G. Della Valle, E. Zojer, *J. Chem. Theory Comput.* **2018**, *14*, 4380.
[20] T. Kamencek, S. Wieser, H. Kojima, N. Bedoya-Martínez, J. P. Dürholt, R. Schmid, E. Zojer, *J. Chem. Theory Comput.* **2020**, *16*, 2716.
[21] V. Coropceanu, R. S. Sánchez-Carrera, P. Paramonov, G. M. Day, J.-L. Brédas, *J. Phys. Chem. C* **2009**, *113*, 4679.
[22] R. Kubo, M. Toda, N. Hashitsume, *Statistical Physics II*, Springer, Berlin **1985**.
[23] C. Melis, R. Dettori, S. Vandermeulen, L. Colombo, D. Fisica, *Eur. Phys. J. B* **2014**, *87*, 96.
[24] E. Lampin, P. L. Palla, P.-A. Francioso, F. Cleri, *J. Appl. Phys.* **2013**, *114*, 033525.
[25] M. Puligheddu, F. Gygi, G. Galli, *Phys. Rev. Mater.* **2017**, *1*, 060802.
[26] Y. He, I. Savić, D. Donadio, G. Galli, *Phys. Chem. Chem. Phys.* **2012**, *14*, 16209.
[27] A. Giri, P. E. Hopkins, *J. Phys. Chem. Lett.* **2017**, *8*, 2153.
[28] W. Shi, J. Chen, J. Xi, D. Wang, Z. Shuai, *Chem. Mater.* **2014**, *26*, 2669.
[29] S. Haas, Y. Takahashi, K. Takimiya, T. Hasegawa, *Appl. Phys. Lett.* **2009**, *95*, 022111.
[30] W. Xie, K. Willa, Y. Wu, R. Häusermann, K. Takimiya, B. Batlogg, C. D. Frisbie, *Adv. Mater.* **2013**, *25*, 3478.
[31] D. Wang, L. Tang, M. Long, Z. Shuai, *J. Phys. Chem. C* **2011**, *115*, 5940.
[32] J. Chen, D. Wang, Z. Shuai, *J. Chem. Theory Comput.* **2012**, *8*, 3338.
[33] G. Schweicher, N. Paquay, C. Amato, R. Resel, M. Koini, S. Talvy, V. Lemaur, J. Cornil, Y. Geerts, G. Gbabode, *Cryst. Growth Des.* **2011**, *11*, 3663.
[34] G. Schweicher, G. Garbay, R. Jouclas, F. Vibert, F. Devaux, Y. H. Geerts, *Adv. Mater.* **2020**, *32*, 1905909.
[35] G. T. Craven, A. Nitzan, *Nano Lett.* **2020**, *20*, 989.
[36] E. Selezneva, A. Vercouter, G. Schweicher, V. Lemaur, K. Broch, A. Antidormi, K. Takimiya, V. Coropceanu, J.-L. Brédas, C. Melis, J. Cornil, H. Sirringhaus, *Adv. Mater.* **2021**, *33*, 2008708.
[37] X. Wang, W. Wang, C. Yang, D. Han, H. Fan, J. Zhang, *J. Appl. Phys.* **2021**, *130*, 170902.
[38] R. Kubo, *Rep. Prog. Phys.* **1966**, *29*, 255.
[39] J. Chen, G. Zhang, B. Li, *Phys. Lett. A* **2010**, *374*, 2392.
[40] F. Müller-Plathe, *J. Chem. Phys.* **1997**, *106*, 6082.
[41] C. Genovese, A. Antidormi, R. Dettori, C. Caddeo, A. Mattoni, L. Colombo, C. Melis, *J. Phys. D: Appl. Phys.* **2017**, *50*, 494002.
[42] X. Wang, J. Zhang, Y. Chen, P. K. L. Chan, *Nanoscale* **2017**, *9*, 2262.
[43] P. Boone, H. Babaei, C. E. Wilmer, *J. Chem. Theory Comput.* **2019**, *15*, 5579.
[44] D. Surblys, H. Matsubara, G. Kikugawa, T. Ohara, *Phys. Rev. E* **2019**, *99*, 51301.
[45] W. H. Press, S. A. Teukolsky, W. T. Vetterling, B. P. Flannery, in *Numerical Recipes*, Cambridge University Press, Cambridge **1992**, pp. 530–600.
[46] A. J. H. McGaughey, M. Kaviany, *Int. J. Heat Mass Transfer* **2004**, *47*, 1799.
[47] J. A. Seijas-Bellido, R. Rurali, J. Íñiguez, L. Colombo, C. Melis, *Phys. Rev. Mater.* **2019**, *3*, 65401.
[48] H. Zhang, G. Lee, K. Cho, *Phys. Rev. B* **2011**, *84*, 115460.
[49] Z. Fan, H. Dong, A. Harju, T. Ala-Nissila, *Phys. Rev. B* **2019**, *99*, 64308.
[50] L. Chen, X. Wang, S. Kumar, *Sci. Rep.* **2015**, *5*, 12763.
[51] P. K. Schelling, S. R. Phillpot, P. Keblinski, *Phys. Rev. B: Condens. Matter Mater. Phys.* **2002**, *65*, 144306.
[52] D. P. Sellan, E. S. Landry, J. E. Turney, A. J. H. McGaughey, C. H. Amon, *Phys. Rev. B* **2010**, *81*, 214305.
[53] H. Zaoui, P. L. Palla, F. Cleri, E. Lampin, *Phys. Rev. B* **2016**, *94*, 54304.
[54] C. Caddeo, C. Melis, M. I. Saba, A. Filippetti, L. Colombo, A. Mattoni, *Phys. Chem. Chem. Phys.* **2016**, *18*, 24318.
[55] N. Kim, B. Domercq, S. Yoo, A. Christensen, B. Kippelen, S. Graham, *Appl. Phys. Lett.* **2005**, *87*, 241908.
[56] J. Callaway, *Phys. Rev.* **1959**, *113*, 1046.